Title
ELASTIC AND INELASTIC SCATTERING OF l6O AND 12C FROM NUCLEI 40 < A < 96

Authors
Becchetti, F.D.
Christensen, P.R.
Manko, V.I.
et al.

Publication Date
1972-09-01

Submitted to Nuclear Physics

LBL-1258
Preprint c.1

ELASTIC AND INELASTIC SCATTERING OF ^{16}O AND ^{12}C FROM NUCLEI $40 \leq A \leq 96$

F. D. Becchetti, P. R. Christensen,
V. I. Manko, and R. J. Nickles

September 1972

AEC Contract No. W-7405-eng-48

DISCLAIMER

ELASTIC AND INELASTIC SCATTERING OF ^{16}O AND ^{12}C FROM NUCLEI $40 \leq A \leq 96$

F. D. Becchetti*

Lawrence Berkeley Laboratory
University of California
Berkeley, California 94720, U.S.A.

and

The Niels Bohr Institute
Copenhagen, Denmark

and

P. R. Christensen, V. I. Manko**, and R. J. Nickles***

The Niels Bohr Institute
Copenhagen, Denmark

September 1972

Abstract

Angular distributions for the elastic scattering of ^{16}O on $^{40,48}Ca$, ^{50}Ti, ^{52}Cr, ^{54}Fe, $^{58,60,62,64}Ni$, $^{86,88}Sr$, $^{92,96}Zr$, and ^{92}Mo at an incident energy of 60 MeV, ^{16}O on ^{96}Zr at 49 MeV, and ^{12}C on ^{96}Zr at 38 MeV have been measured using a ΔE-E counter telescope. Inelastic scattering of ^{16}O on ^{48}Ca, ^{54}Fe, ^{58}Ni, ^{88}Sr, ^{96}Zr (60 MeV) and ^{12}C on ^{96}Zr (38 MeV) populating low lying collective states of the target was also measured.

The elastic scattering angular distributions are characteristic of those for strongly absorbed particles. The inelastic data show structure, however, which is found to be due to the destructive interference between Coulomb and nuclear excitation. The data are analyzed using the optical model with collective formfactors. Deformation parameters in good agreement with those obtained by other means can be extracted provided corrections for the finite size of the projectile are made.

---

*N. S. F. Fellow 1970/71

**Permanent address: Kurchatov Institute, Moscow, U.S.S.R.

***James A. Picker Fellow, 1969/71. Present address: University of Wisconsin, Madison, Wisconsin, U.S.A.

1. Introduction

The usefulness of heavy ion projectiles in the study of inelastic scattering at sub-Coulomb incident energies has been demonstrated[1]). The mechanism at these energies is excitation due solely to Coulomb interactions, i.e., Coulomb excitation[2]).

In this paper we report the study of elastic and inelastic scattering of oxygen and carbon ions from nuclei $40 \leqslant A \leqslant 96$ at incident energies above the Coulomb barrier. The results are analyzed using the optical model and DWBA. It will be shown that the shape of the inelastic scattering angular distributions are mainly determined by interference between Coulomb and nuclear excitation and that heavy ions can be used as a sensitive probe of the ion-ion potential.

2. Experimental Methods

The experiments were performed at the Niels Bohr Institute tandem laboratory. The heavy ion beams were provided by an HVEC model FN tandem Van de Graaff accelerator. The measurements described here were obtained as part of a more extensive experiment designed to study particle transfer reactions with heavy ions[3]). The experimental techniques are described in more detail elsewhere[3]).

The elastic and some of the inelastic scattering data were obtained with an array of 100 μm Si surface barrier (SiSB) counters, while most of the inelastic measurements were made using a ΔE-E SiSB counter telescope (13 or 20 μm ΔE and 100 μm E counters, respectively). The mass resolution was between 6 and 10% for the telescope. The energy resolution (FWHM) was 200-400 keV.

An ^{16}O spectrum obtained from the bombardment of ^{96}Zr with 60 MeV ^{16}O ions is shown in fig. 1. The group corresponding to 1.8 MeV excitation energy is an unresolved doublet due to excitation of the first 2^+ and 3^- levels in ^{96}Zr. With the exception of ^{96}Zr the first collective levels of the other target nuclei studied could be resolved.

The elastic data presented here include: $^{40,48}Ca$, ^{50}Ti, ^{52}Cr, ^{54}Fe, $^{58,60,62,64}Ni$, $^{86,88}Sr$, $^{92,96}Zr$, ^{92}Mo + ^{16}O(60 MeV); ^{96}Zr + ^{16}O(49 MeV); ^{96}Zr + ^{12}C(38 MeV). The inelastic data include: ^{48}Ca, ^{54}Fe, ^{58}Ni, ^{88}Sr, $^{96}Zr(^{16}O,^{16}O')$, E_L = 60 MeV and $^{96}Zr(^{12}C,^{12}C')$, E_L = 38 MeV.

3. Elastic Scattering

3.1 DATA

The elastic scattering data are shown in figs. 2, 3, 4 as ratio to Rutherford, $\sigma(\theta)/\sigma_R(\theta)$. The angular distributions vary systematically with target or projectile Z and the beam energy. As shown in ref. 3, the elastic angular distributions can be approximated by a simple function of the apsidal distance[4])

$$D(\theta) = \eta/k\ (1 + \csc \frac{\theta}{2}) \tag{3.1}$$

where $\eta/k = Z_1 Z_2 e^2/2E_{c.m.}$. Z_1 and Z_2 are the charges of the projectile and target, respectively, $E_{c.m.}$ is the c.m. energy, and θ is the c.m. scattering angle. The decrease from Rutherford scattering begins at an angle such that $D(\theta) \approx 1.7\ (A_1^{1/3} + A_2^{1/3})$ fm where A_1 and A_2 are the projectile and target mass numbers, respectively.

3.2 OPTICAL MODEL ANALYSIS

The elastic scattering data have been analyzed using the optical model (OM) with a potential of the form:

$$U(r) = [V_R(r) + iW_I(r)] + V_C(r)$$

where

$$V_R(r) = V_R\ f(r) = V_R\left(1 + \exp \frac{r-R_R}{a_R}\right)^{-1} \tag{3.2}$$

and

$$W_I(r) = W_I\ g(r) = W_I\left(1 + \exp \frac{r-R_I}{a_I}\right)^{-1}$$

The Coulomb potential $V_C(r)$ was taken to be that due to uniformly charged spheres with a separation $R_c = 1.3\ (A_1^{1/3} + A_2^{1/3})$ fm.

The parameters V_R, R_R, a_R, W_I, R_I, a_I were obtained by griding on the parameters and comparing the calculations with the data. Calculations were performed with the programs GAP5[6]) and DWUCK[7]). Up to 140 partial waves were used. This corresponds to 3-6 times the ℓ-values for which T_ℓ, the transmission coefficient[5]) for the ℓth partial wave is $\sim 1/2$. The differential equations were integrated out to 40 fm in 0.1 fm steps. The integration routines used in the programs were found to diverge for steps much smaller or greater than this value. The value 0.1 fm is on the order of $\lambda/8$, where λ is the asymptotic wave length of the projectile.

It was found in fitting the data that the calculations for $\sigma/\sigma_R > 0.1$ were most sensitive to the optical potentials in the region $r \gtrsim 9$ fm, and furthermore that in this region it was necessary that the potentials fall off exponentially.

One family of parameters was obtained using the following restrictions:

$$R_R = R_I = R_0 = r_0(A_1^{1/3} + A_2^{1/3})$$
$$a_R = a_I = a_0 \qquad (3.3)$$

The parameters V_R, W_I, r_0, and a_0 were adjusted to fit the data. It was found that all the data could be reasonably well fitted with a standard set of parameters (set I), although improvements could be obtained in some cases by adjusting V_R slightly (set II). The resulting parameter sets (OM sets I, II) are listed in table 1 and the OM fits to the data are shown in figs. 2, 3, and 4.

We have also fitted ^{58}Ni, $^{96}Zr + ^{16}O$ with a potential (set III) having a smaller radius than for sets I and II. The fits are shown in fig. 5.

Finally, an optical potential, generated by folding a nucleon-projectile optical potential with the target nucleon distribution, was considered[8,9]. This was approximated with a Woods-Saxon form with $R_0 = r_0 A_2^{1/3}$ and diffuseness $a_0 = 1$ fm. The main differences between the "folded" type potential and that given by 3.3 are that for the former $R_0 \propto A_2^{1/3}$ while for the latter $R_0 \propto (A_1^{1/3} + A_2^{1/3})$, and that the folded type potential has a much larger diffuseness[9]. The parameters obtained by fitting the ^{96}Zr, $^{58}Ni + ^{16}O$ data with the folded type potential are given in table 1 (set IV). The fits to the data are shown in fig. 5. In obtaining the fits, we have constrained $R_R = R_I = r_0 A_2^{1/3}$ and $a_R = a_I = 1$ fm. Also, the exact folded potential is not as simple as the Woods-Saxon form used here[9].

In figs. 6 and 7, we compare the OM potentials, which fit the $^{96}Zr+^{16}O$ elastic data. It can be seen in fig. 6 that the real part of potential sets I and III are very similiar for $r > 9$ fm, whereas set IV, while having a much larger diffusivity, intersects the other potentials at $r \approx 11$ fm. The absorptive potentials (fig. 7) show a similiar behavior although not so pronounced as that for the real potentials.

In figs. 6 and 7, the calculated and experimental elastic angular distributions for 49 and 60 MeV ^{16}O on ^{96}Zr are shown versus the classical distance of closest approach (eq. 3.1). It is seen that the region $r \approx 11$ fm just corresponds to the region in which the data are fitted and for which the OM calculations are most alike.

We conclude that elastic scattering can be used to determine the ion-ion optical potentials in the surface region corresponding to grazing collisions and that $W(r)/V(r) \sim 1:2.5$ in this region. The precise shapes of the potentials are not well determined, however. Also, since our analysis is sensitive to a region $r \gtrsim 9$ fm, it is not possible to deduce information about interior features of the potentials, such as a repulsive core[10]. As we shall show in section 4.3, the study of inelastic scattering can help determine the shpaes of the potentials.

3.3 COMPARISON WITH OTHER ANALYSES

We may compare our results with those of refs.[11,12,13] for $^{40}Ca+^{16}O$, E_L = 20 to 47 MeV. The optical potentials used in these references are listed in table 2. If one compares the values of the real and imaginary potentials at r = 9.2 fm, which corresponds to r = 11 fm in the $^{96}Zr + ^{16}O$ system, we find (table 2) that the values of V(r) are similiar, but that the slopes differ, whereas, the values of W(r) vary considerably.

Some of the elastic data presented here have also been analyzed[14] using the smooth cut-off model and a semi-classical model[3], but these analyses will not be discussed here.

4. Inelastic Scattering

4.1 ANGULAR DISTRIBUTIONS

Angular distributions for the inelastic scattering of ^{16}O-ions have been obtained on the ^{48}Ca, ^{54}Fe, ^{58}Ni, ^{88}Sr, and ^{96}Zr target nuclei at 60 MeV and ^{12}C on ^{96}Zr at 38 MeV (figs. 8-10). The most striking feature is an oscillation which appears to be correlated with the rise of the elastic data above Rutherford scattering. Similiar effects have been observed in the inelastic scattering of τ and α-particles[15,16]).

The oscillation is most pronounced on the ^{96}Zr, ^{58}Ni and, probably, ^{48}Ca target nuclei, though for the latter the rise at forward angles was impossible to measure, due to a very strong background of the elastically scattered ^{16}O ions on the ^{16}O and ^{12}C impurities in the target. Results of a study of this effect in the excitiation function of ^{16}O + ^{58}Ni inelastic scattering have been published elsewhere[17]).

4.2 SEMI-CLASSICAL MODEL

The observed behaviour of the angular distributions can be explained qualitatively as an interference between Coulomb excitation and nuclear excitation[17]). In the semi-classical description of the collision the particle is moving along a classical trajectory, and one may write the cross section for excitation of a collective state, in first order perturbation theory as:

$$d\sigma_{inel}\,(\theta) = P(\theta)\; d\sigma_{el}\,(\theta) \qquad (4.1)$$

where $P(\theta)$ is the probability that the nucleus is excited in a collision in which the particle is scattered into an angle θ and $d\sigma_{el}\,(\theta)$ is the elastic cross section.

The probability $P(\theta)$ can be expressed in terms of the amplitude $b(\theta)$ for a transition from the ground state to the excited state as:

$$P(\theta) \propto [b(\theta)]^2 \tag{4.2}$$

As the total interaction potential between the colliding particles is of the form (see section 3.2):

$$V_C(r) + V_R f(r) + iW_I\, g(r)$$

with V_R and W_I negative (attractive and absorptive, respectively) and $V_C(r)$ positive (repulsive), one may write (neglecting the summation over the different m-states):

$$b(\theta) = [b_C(\theta) - b_R(\theta)] - ib_I(\theta) \tag{4.3}$$

where b_C, b_R, and b_I (all real and positive) are the amplitudes due to the Coulomb field, the real nuclear field, and the absorptive field, respectively.

Since $\theta = \theta(D)$, D being the apsidal distance (eq. 3.1), one has that

$$d\sigma_{inel}(D) \propto d\sigma_{el}(D) \left[[b_C(D) - b_R(D)]^2 + b_I(D)^2\right] \tag{4.4}$$

At large distances that is at forward angles, the Coulomb amplitude is dominant, and the cross-section is pure Coulomb excitation. With decreasing distance, that is with increasing angle, the amplitudes b_R and b_I will increase faster than the Coulomb amplitude b_C and destructive interference between the Coulomb amplitude b_C and the nuclear amplitude b_R occurs, giving rise to an oscillation in the inelastic cross section. Finally, the rapid decrease of $d\sigma_{el}$ at large angles, which is due to the absorption, results in the fall off of the cross section. The probability $P(\theta)$ continues to rise, however, approaching unity at large angles. For this situation perturbation theory may not be valid.

We illustrate the features outlined above by plotting $d\sigma_{inel}(D)/d\sigma_{el}(D)$ and the square of the formfactor (see section 4.3) for ^{12}C, ^{16}O on ^{96}Zr leading to the unresolved 2^+ and 3^- states in ^{96}Zr at about 1.8 MeV excitation energy versus $D(\theta)$ and r, respectively. This is shown in fig. 11. Optical potential set II has been used with the quantities B(EL) and β_L^N adjusted to fit the data. The formfactor shown in fig. 11 is for the L=3 $^{96}Zr(^{16}O,^{16}O)^{96}Zr(3^-)$ transition, as it is found to be responsible for most of the cross section. It can be seen from fig. 11 that the shape of P(D) is strongly correlated with $|F_L(D)|^2$ and in particular, the minimum corresponding to the cancellation of the real parts of $F_L^C(r)$ and $F_L^N(r)$ at $D \doteq r = 12$ fm. One finds a behaviour similar to that shown in fig. 11, when D is changed by fixing θ and varying the bombarding energy as in ref. 17.

The interpretation of the observed oscillations as due to destructive interference is supported by the DWBA calculations shown in fig. 8. In this figure we show data for $^{96}Zr(^{12}C,^{12}C')$ to the states at 1.8 MeV (2^+ and 3^-). Also shown are DWBA calculations using only the Coulomb part and only the nuclear part of the formfactor (top) and the total formfactor (bottom) with B(EL) and β_L^N adjusted to fit the data (see section 4.3).

4.3 DWBA CALCULATIONS

We have performed DWBA calculations using the program DWUCK[7]) and the formfactor given by [18,19])

$$F_L(r) = F_L^C(r) + F_L^N(r)$$

where

$$F_L^C(r) = \frac{eZ_1 \; 4\pi\sqrt{B(EL)}}{2L+1} \; \frac{1}{r^{L+1}} \tag{4.5}$$

and

$$F_L^N(r) = \beta_L^N \left(V_R R_R \frac{df(r)}{dr} + iW_I R_I \frac{dg(r)}{dr} \right)$$

The quantity B(EL) is the e.m. transition probability for a $0^+ \rightarrow L$ electric excitation of the target and β_L^N is the multipole deformation of the nuclear optical potential. Up to 140 partial waves were used with the numerical integrations taken out to 40 fm in o.1 fm steps. This is adequate (± 10%) in the region D $\lesssim$ 15 fm, which included most of the data points.

The values of B(EL) were taken from the values compiled by Bernstein[20]) or from other sources. Where direct measurements of the electric transition rates were not available we have deduced values from the potential deformation parameters determined from inelastic scattering using light ions. The values of β_L^N are determined by fitting the data. Unlike the situation for light ions where only the magnitude of the DWBA cross section depends on β_L^N, for heavy ions both the magnitude and shape of the angular distributions change, due to the interference terms.

In figs. 8-10, we show the fits to the inelastic data using OM potential set II. The values of β_L^N obtained are listed in table 3, together with the B(EL) values. In fig. 12 and table 3, we also show the results of calculations for ^{96}Zr, ^{58}Ni + ^{16}O using OM sets III and IV. It can be seen that OM sets II and III yield similar fits to the data, whereas, OM set IV gives a much worse fit. This is due to the large diffuseness (a_0 = 1 fm) for this potential which greatly affects the derivative term appearing in the formfactor. The fits to the inelastic data suggest that the appropriate OM potentials have a diffuseness parameter, a_0, ≈ 0.5 fm.

Better agreement with the experimental angular distributions, particularly at forward angles, can be obtained by adjusting B(EL). This is shown in fig. 8 for the 1.8 MeV states observed in $^{96}Zr(^{12}C,^{12}C')$. In some cases this may be justified, in that direct measurements of B(EL) are not available.

4 4 THE PHASE OF THE NUCLEAR FORMFACTOR

It has been suggested that interference effects can be used as a unique probe in determining the proper phase of the nuclear part of the transition amplitude[22]). As can be seen from eqs. 4.3 and 4.5, the imaginary part of $F_L^N(r)$ results in an amplitude which adds incoherently to the inelastic cross section. The simple collective form factor used in eq. 4.5 has $\mathrm{Im}\, F_L^N(r)/\mathrm{Re}\, F_L^N(r) = W_I/V_R$ or about 1:2.5 for the potentials used. The contribution of $\mathrm{Im}\, F_L^N(r)$ is most important at the minimum in the cross section corresponding to $b_C(\theta) = b_R(\theta)$. The analysis of the inelastic data is consistent with the phase of the formfactor given by the collective model (eq. 4.5).

4.5 FINITE SIZE CORRECTIONS

In electron or light-ion inelastic scattering, the deformation of the interaction potential can be expected to be nearly the same as the mass deformation of the target owing to the small projectile size. This is not expected to be the case when the projectile size is large, as it is for heavy ions. Averaging the interaction over the projectile nucleon distribution will result in a projectile-nucleus potential deformation which will be smaller than that of the target nuclear state involved. This effect has been observed for inelastic alpha scattering[20]. It is found that one can deduce the target state mass deformation from the OM potential deformation using the relation

$$\beta_M R_M = \beta_L^N R_0 \tag{4.6}$$

where β_M, β_L^N and R_M, R_0 are the deformations and radii of the target and optical model potentials, respectively. Eq. 4.6 has been used to deduce target mass deformations from the observed OM potential deformations, β_L^N. The results are listed in table 3.

Since the finite size corrections appear to be quite substantial, a more exact treatment than that given by (4.6) would be desirable.

4.6 COMPARISON WITH OTHER MEASUREMENTS

In table 3, we compare the potential and mass deformations obtained from the analysis of heavy ion inelastic scattering with deformation parameters obtained from other methods, such as (α,α'). The deformation parameters obtained in the latter measurements should be compared with the β_M values deduced in this experiment. The agreement in most cases is good, the β values being within ± 10% of each other.

5. CONCLUSIONS

The present results indicate that the DWBA treatment may be applied to heavy ion reactions well above the Coulomb barrier and by utilizing the interference between Coulomb and nuclear forces, one may use heavy ions as a sensitive probe of these forces.

6. ACKNOWLEDGMENTS

The authors thank A. Winther, S. Landowne, and R. Broglia for useful information and discussions. F.D.B., V.J.M., and R.J.N. acknowledge the hospitality provided by the staff of the Niels Bohr Institute during their stay at the Institute.

References

1) Proc. of the Conf. on Nucl. Reactions Induced by Heavy Ions, eds. W. Hering and R. Bock (North Holland, 1970). Chap. X, and references cited therein

2) K. Alder, A. Bohr, T. Huus, B. Mottelson, and A. Winther, Rev. Mod. Phys. 28 (1956) 432 and references cited therein

3) R. J. Nickles, V. I. Manko, P. R. Christensen, and F. D. Becchetti, Phys. Rev. Lett. 26 (1971) 1267

P. R. Christensen, *et al.*, Proc of the Intl. Conf. on Heavy Ion Physics, Dubna, 1971, p. 235

P. R. Christensen, V. I. Manko, F. D. Becchetti, and R. J. Nickles, submitted to Nucl. Phys.

4) R. D. Evans, *The Atomic Nucleus* (McGraw-Hill, New York, 1955) p. 845

5) P. E. Hodgson, *The Optical Model of Elastic Scattering* (Oxford University Press, London, 1963)

6) GAP5, Birthe Olsen, unpublished.

7) DWUCK, written by P. D. Kunz, University of Colorado reports COO-535-606 and COO-535-613, unpublished. A modified version of the program described in these reports was used

8) G. W. Greenlees, G. J. Pyle, and Y. C. Tang, Phys. Rev. 171 (1968) 1115

9) S. G. Kadmenskii, *et al.*, Yad. Fiz. 10 (1969) 730. [(English transl.: Soviet J. Phys. 10 (1970) 422]

10) H. A. Bethe, Phys. Rev. 167 (1968) 879

K. A. Brueckner, *et al.*, Phys. Rev. 171 (1968) 1188

W. Scheid, R. Ligensa, and W. Greiner, Phys. Rev. Lett. 21 (1968) 1479

11) J. S. Eck, R. A. LaSalle, and D. A. Robson, Phys. Rev. 186 (1969) 1132

12) M. C. Bertin, et al., Nucl. Phys. A167 (1971) 216

13) J. Orloff and W. W. Daehnick, Phys. Rev. C3 (1971) 430

14) F. D. Becchetti, et al., Proc. of the Intl. Conf. on Heavy Ion Physics, Dubna, 1971, p. 361

15) F. T. Baker and R. Tickle, Phys. Rev. C5 (1972) 544

16) M. Samuel and U. Smilansky, Phys. Lett. 28B (1968) 318
R. J. Pryor, T. X. Saladin, R. H. Bassel, and R. M. Drisko, ref. 1, p. 450
B. Wakefield, et al., Phys. Lett. 31B (1970) 56

17) F. Videbaek, I. Chernov, P. R. Christensen, and E. E. Gross, Phys. Rev. Lett. 28 (1972) 1072. R. Broglia, et al., Phys. Lett. 40B (1972) 293

18) R. H. Bassel, G. R. Satchler, R. M. Drisko, and E. Rost, Phys. Rev. 128 (1962) 2693

19) C. Leclercq-Willain, ref. 1, p. 453

20) A. M. Bernstein, in Adv. in Nucl Phys., eds. M. Baranger and E. Vogt, 3 (1969) 325

21) J. Y. Park and G. R. Satchler, Particles and Nuclei, 1 (1971) 233

22) G. R. Satchler, Phys. Lett. 33B (1970) 385

23) P. H. Stelson and L. Grodzins, Nucl. Data 1 (1966) 21

24) E. P. Lippincott and A. M. Bernstein, Phys. Rev. 163 (1967) 1170

25) F. Hinterberger, et al., Nucl. Phys. A115 (1968) 570

26) M. Inoue, Nucl. Phys. A119 (1968) 449

27) E. R. Flynn, D. D. Armstrong, and J. G. Beery, Phys. Rev. C1 (1970) 703

Table 1. Optical Model Parameters[a)]

Set	E_L, MeV	Projectile	Target	V_R, MeV	W_I, MeV	R_0, fm	a_0, fm	Comments
I.	49,60	^{16}O	^{40}Ca-^{96}Zr	-40	-15	$1.30(A_1^{1/3} + A_2^{1/3})$	0.50	General set
	38	^{12}C	(see figs. 2-4)					
II.	60	^{16}O	^{52}Cr	-35	Same as Set I			V_R adjusted
			^{54}Fe, $^{58,60}Ni$	-25				
			^{92}Zr, ^{92}Mo	-22				
III.	60	^{16}O	^{58}Ni	-320	-90	$1.10(A_1^{1/3} + A_2^{1/3})$	0.50	r_0= 1.10 fm
			^{96}Zr	-620				
IV.	60	^{16}O	^{58}Ni	-230	-120	$1.15\ A_2^{1/3}$	1.00	Folded-type
			^{96}Zr	-360				potential

[a)] $U(r) = (V_R + iW_I)\left(1 + \exp\frac{r-R_0}{a_0}\right)^{-1} + V_c(r)$ where $V_c(r)$ is the Coulomb potential due to uniformly charged spheres with $R_c = 1.30(A_1^{1/3} + A_2^{1/3})$ fm.

Table 2. Optical Model Parameters for $^{16}O + ^{40}Ca$

E_L, MeV	V_R, MeV	W_I, MeV	R_0, fm	r_0, fm [a]	a_0, fm	V_R(9.2fm) [b] MeV	W_I(9.2fm) [b] MeV	Ref.
38-42	- 35	- 2.0	7.20	1.19	0.60	-1.21	-0.069	11
	- 30	- 1.5	7.20	1.19	0.70	-1.63	-0.081	
20-40	-150	-10	7.40	1.23	0.467	-3.11	-0.21	12
40	- 91.7	-43.7	7.72	1.28	0.406	-2.33	-1.11	13
47	- 62.9	- 4.46	7.72	1.28	0.399	-1.50	-0.11	
60	- 40	-15	7.85	1.30	0.50	-2.52	-0.94	This study.

a) $r_0 \equiv R_0/(A_1^{1/3} + A_2^{1/3})$. See also footnote a) table 1.

b) The potentials at r = 9.2 fm, corresponding to $r = 1.55(A_1^{1/3} + A_2^{1/3})$ fm.

Table 3. Deformation Parameters

Nucleus	Ex,[a] MeV	J^{π} [a]	OM Set	B(EL)[b] s.p.u.	β^N_L [c]	β_M [d]	Other Meas.[e]		Ref.
60 MeV ^{16}O									
^{48}Ca	3.83	2^+	I	1.7	0.06	0.10	0.13	(α,α')	24
	4.50	3^-	I	5.4	0.08	0.134	(0.18)[g]		
^{54}Fe	1.40	2^+	II	8.7	0.088	0.147	0.18	(d,d')	25
	3.00	2^+	II	3.0	0.08	0.134	0.14	(d,d')	25
^{58}Ni	1.45	2^+	II	9.9	0.092	0.152	0.188	(α,α')	26
			III	9.9	0.187	0.26			
			IV	9.9	0.086	0.075			
	3.20[f]	2^+	II	1.2	(0.044)[f]	(0.074)[f]	0.049	(α,α')	26
		2^+		2.3			0.049	(α,α')	26
	4.50	3^-	II	13.3	0.12	0.198	0.16	(α,α')	26
^{88}Sr	1.84	2^+	I	8.5	0.085	0.133	(0.12)[g]		
^{96}Zr	1.8[f]	2^+	I	(2)[h]			0.06	(t,t')	27
		3^-		(17)[h]	0.12	0.186	0.165	(t,t')	27
		3^-	III		0.148	0.192			
		3^-	IV		0.230	0.202			

(continued)

Table 3 (continued)

Nucleus	Ex,[a] MeV	J^{π}[a]	OM Set	B(EL)[b] s.p.u.	β_L^N[c]	β_M[d]	Other Meas.[e]		Ref.
38 MeV ^{12}C									
^{96}Zr	1.8	2^+	I	$(2)^h$			0.06	(t,t')	27
		3^-		$(17)^h$	0.122	0.189	0.165	(t,t')	27
		2^+	I	$(5)^i$			0.06	(t,t')	27
		3^-		$(17)^h$	0.099	0.155	0.165	(t,t')	27

a) The excitation energies are estimated to be accurate to ± 50 keV. The spins and parities assumed are shown and are taken from the references cited.

b) The e. m. transition probability for the target state as determined from (e,e') or Coulomb excitation. The values are taken from the compilation of ref. 20, unless otherwise noted, and are given in single particle units.

c) The potential deformation β_L^N (eq. 4.5).

d) The target mass deformation deduced from β using eq. 4.6 with $R_m = 1.3\ A_2^{1/3}$ fm.

e) Other measurements of potential or mass deformation. These should be compared to β_M.

f) Unresolved group of states. The J^{π} of the state(s) most likely to be excited in heavy-ion inelastic scattering is given.

(continued)

Table 3 (continued)

g) From compilation of ref. 23.

h) Deduced from (t,t') measurements of ref. 27.

i) Adjusted to fit the data at forward angles (see fig. 8).

Figure Captions

Fig. 1. An ^{16}O spectrum from $^{16}O + {}^{96}Zr$.

Fig. 2. Elastic scattering of ^{16}O at 60 MeV (lab). Optical calculations are shown for sets I and II from table 1.

Fig. 3. Same as fig. 2.

Fig. 4. Elastic scattering of $^{16}O + {}^{96}Zr$ (49 MeV) and $^{12}C + {}^{96}Zr$ (38 MeV). Optical model calculations for set I, table 1 are shown.

Fig. 5. Elastic scattering of $^{16}O + {}^{58}Ni$, $^{16}O + {}^{96}Zr$ at 60 MeV (lab). Optical model calculations for sets III, IV, table 1 are shown.

Fig. 6. Left: The real part of the optical potentials which fit $^{16}O + {}^{96}Zr$ elastic scattering (table 1, figs. 3-5). Note that the origin starts at r = 4 fm. $V_C(r)$ is the Coulomb potential. Right: The elastic data for $^{16}O + {}^{96}Zr$ at 49(•) and 60(∘) MeV as ratio to Rutherford scattering, versus $D(\theta)$ (eq. 3.1). The curves are optical model calculations for the potentials indicated (E_L = 60 MeV).

Fig. 7. Same as fig. 6 but for the absorptive part of the OM potential.

Fig. 8. Top: The data for $^{12}C + {}^{96}Zr$ populating the unresolved 2^+ and 3^- levels at 1.8 MeV excitation energy. The calculations shown are for the Coulomb and nuclear parts of the formfactor (eq. 4.5). Bottom: the solid line is the DWBA calculation using the sum of the Coulomb and nuclear parts of the form factor with B(EL) and β_L^N adjusted (see table 3). The dashed line corresponds to values of B(EL) taken from other measurements (see table 3).

Fig. 9. The inelastic scattering of ^{16}O ions at 60 MeV. DWBA calculations are shown with the formfactor parameters (eq. 4.5) listed in table 3. Optical model sets I and II were used.

Fig. 10. Same as fig. 9. Optical model sets I and II were used.

Fig. 11. Top: The ratio of inelastic to elastic scattering for $^{16}O + {}^{96}Zr$ and $^{12}C + {}^{96}Zr$ populating the 2^+ and 3^- states at 1.8 MeV excitation energy. The DWBA calculation is for the formfactor shown. $D(\theta)$ is the apsidal distance for the angle θ (eq. 3.1). Bottom: The formfactor for $^{12}C + {}^{96}Zr$ (3^-) as given by eq. 4.5 with B(EL) and β_L^N adjusted to fit the data.

Fig. 12. Same as fig. 9 except optical model sets III and IV were used. The parameters are listed in table 3.

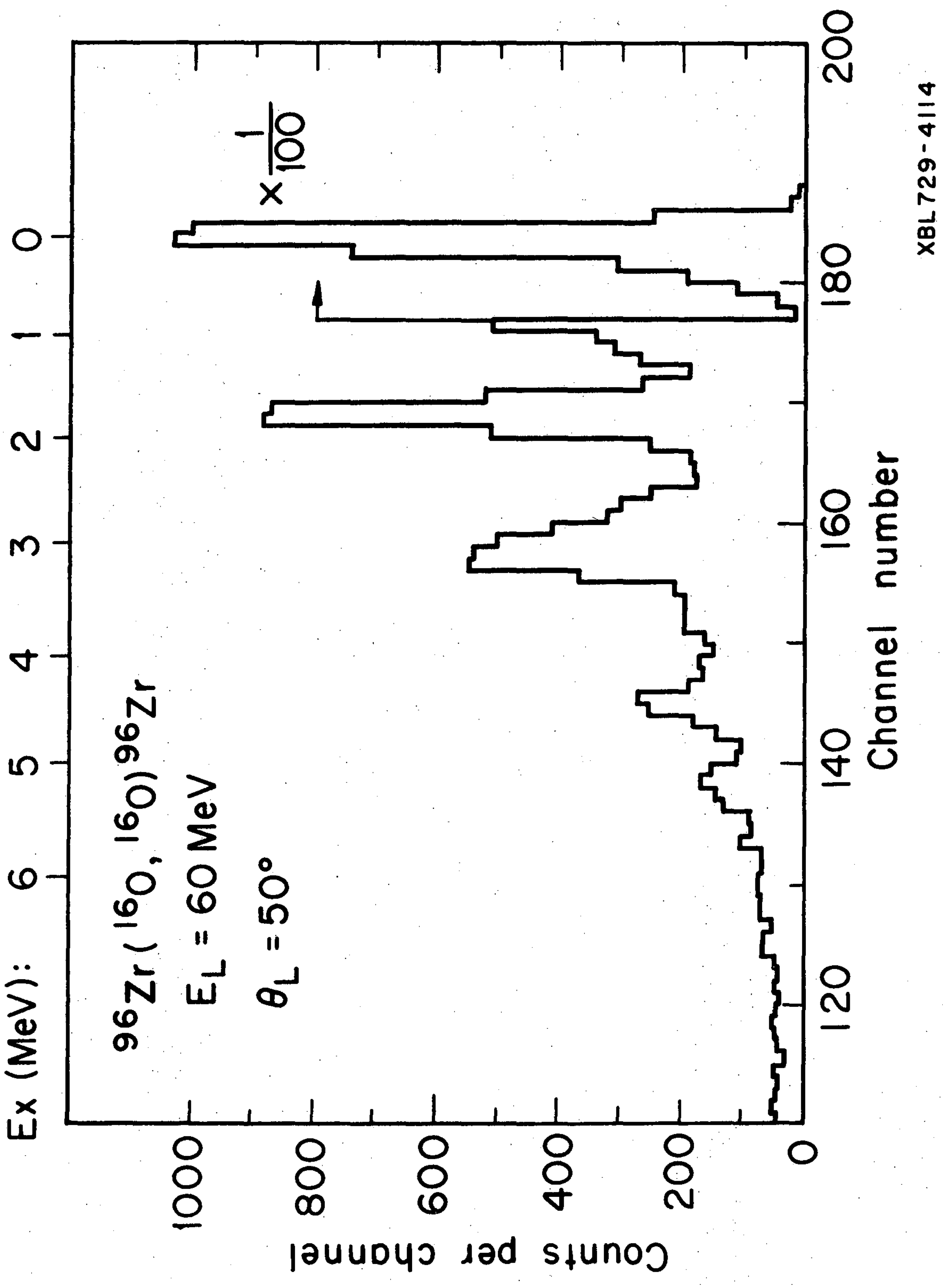
Ex (MeV):
0
1
2
3
4
5
6
$^{96}Zr(^{16}O, ^{16}O)^{96}Zr$
$E_L = 60$ MeV
$\theta_L = 50°$
$\times \frac{1}{100}$
Counts per channel
0
200
400
600
800
1000
Channel number
120
140
160
180
200
XBL 729-4114

Fig. 1

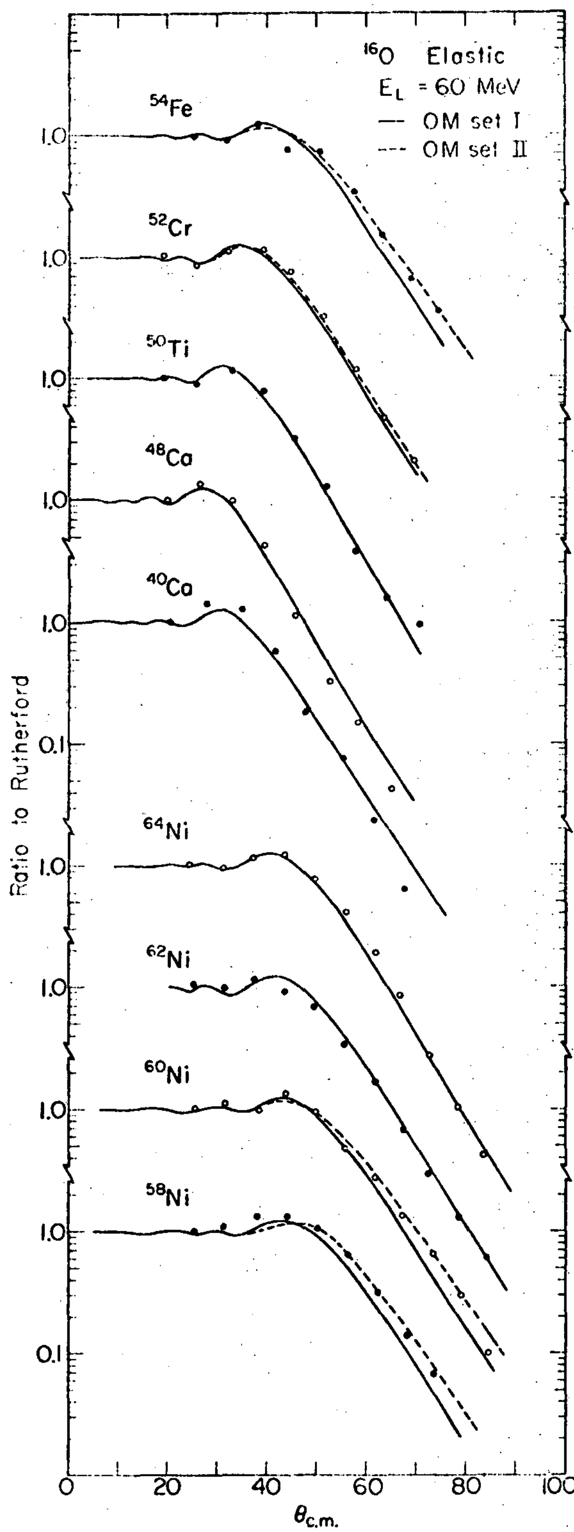

^{16}O Elastic
E_L = 60 MeV
— OM set I
--- OM set II
^{54}Fe
^{52}Cr
^{50}Ti
^{48}Ca
^{40}Ca
^{64}Ni
^{62}Ni
^{60}Ni
^{58}Ni
1.0
0.1
Ratio to Rutherford
0
20
40
60
80
100
$\theta_{c.m.}$
XBL723-2612

Fig. 2

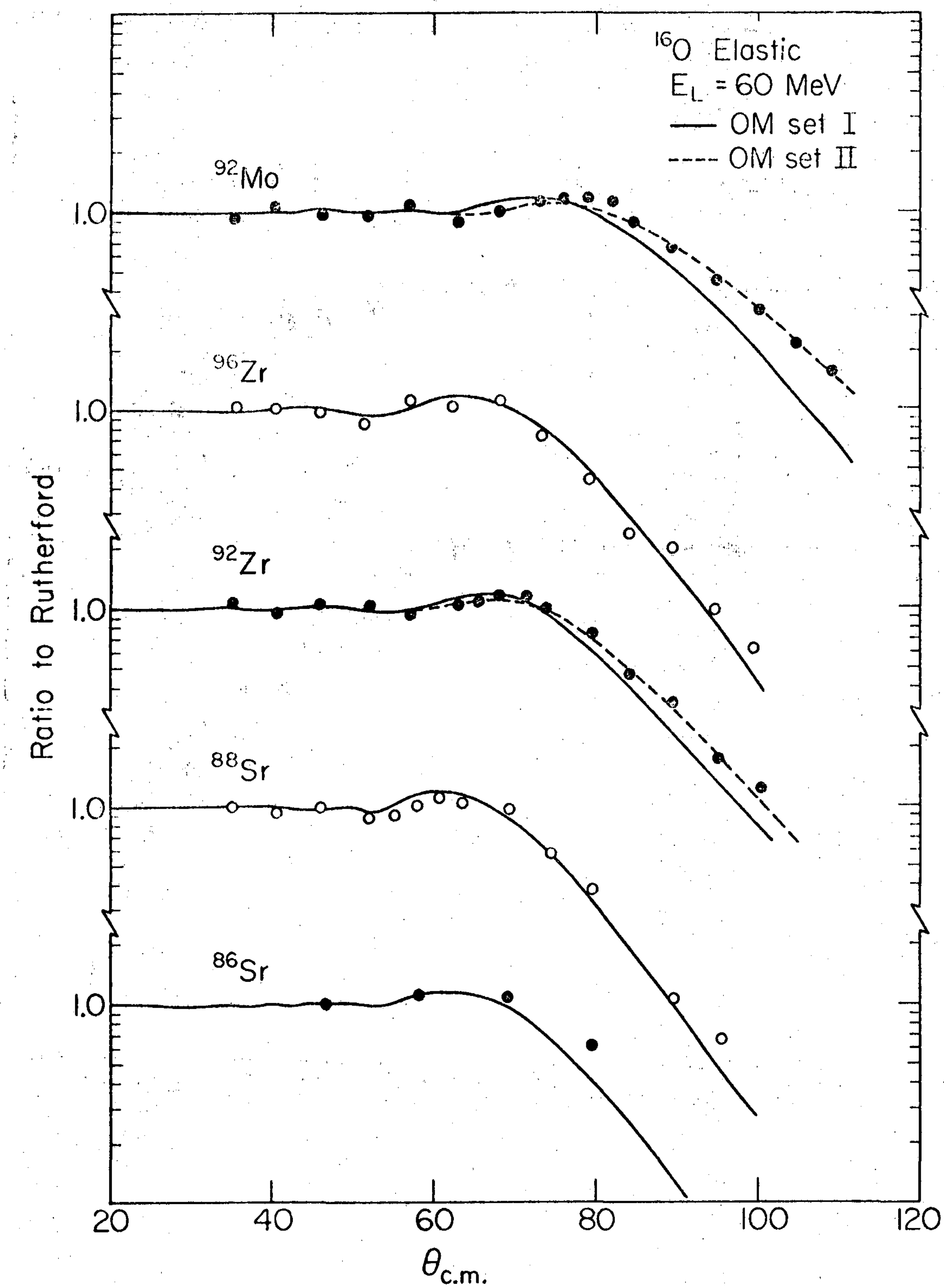

XBL723-2611

Fig. 3

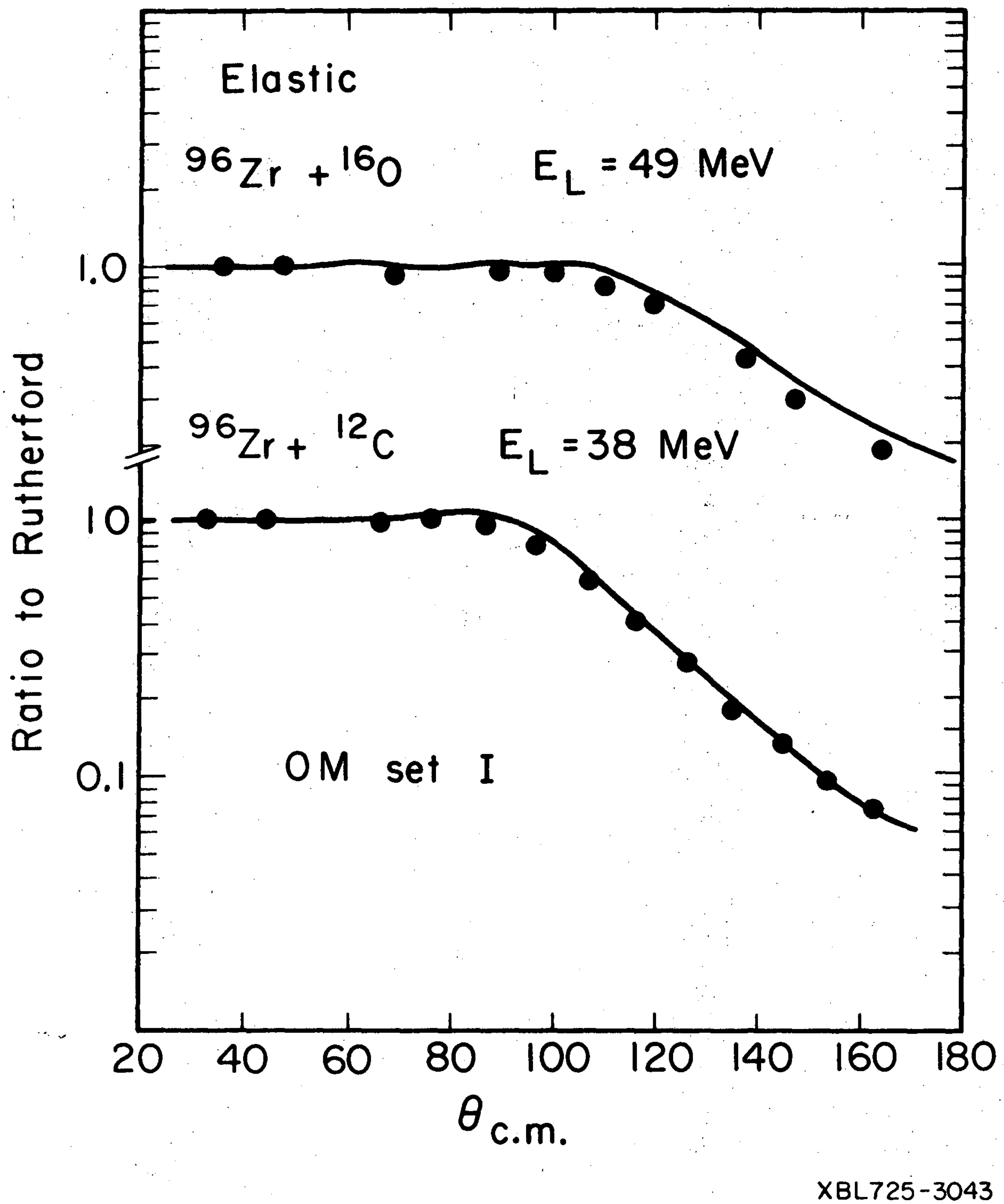
Elastic
$^{96}Zr + ^{16}O$
$E_L = 49$ MeV
$^{96}Zr + ^{12}C$
$E_L = 38$ MeV
OM set I
1.0
1.0
0.1
Ratio to Rutherford
20
40
60
80
100
120
140
160
180
$\theta_{c.m.}$
XBL725-3043

Fig. 4

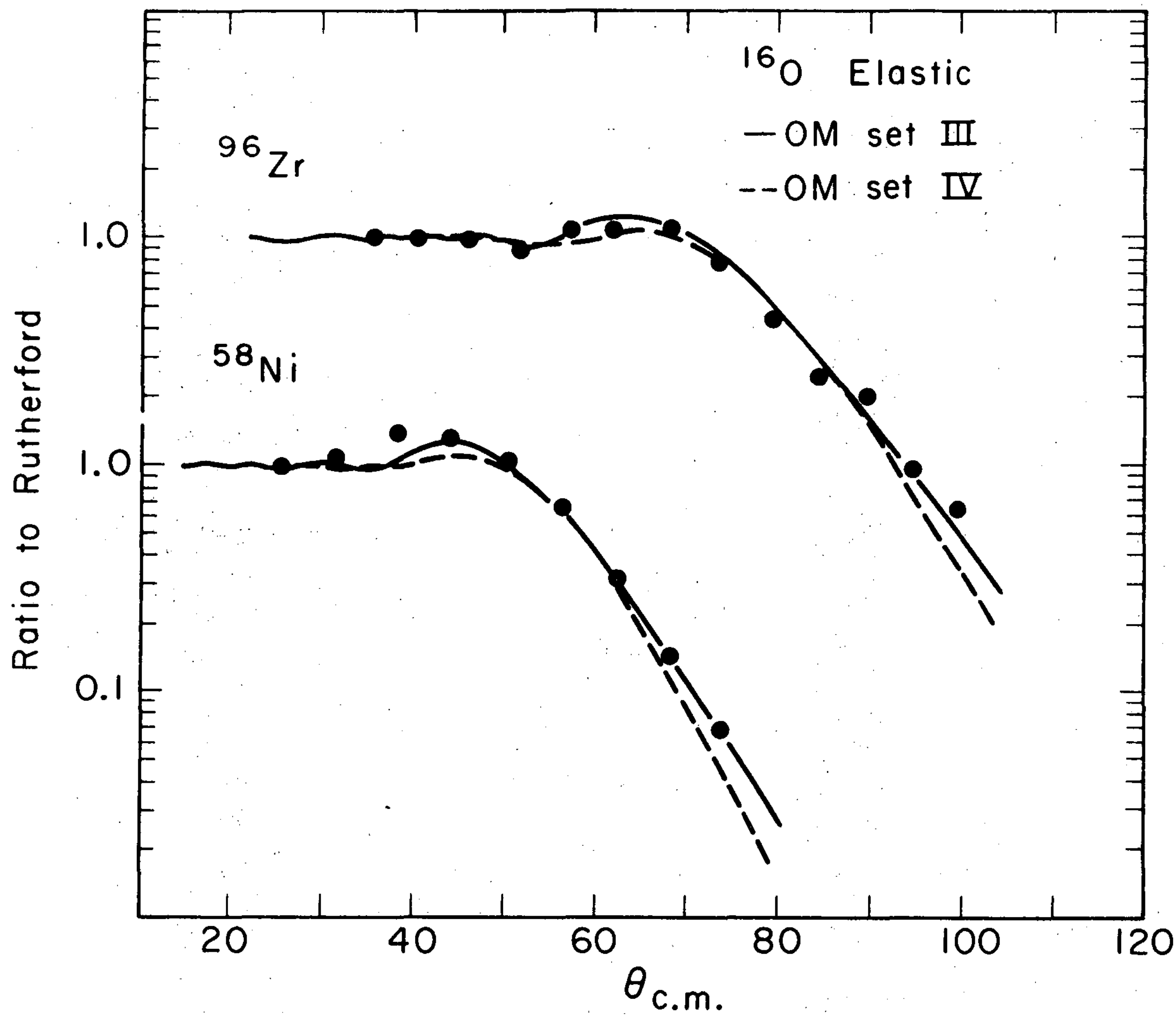

XBL725-3044

Fig. 5

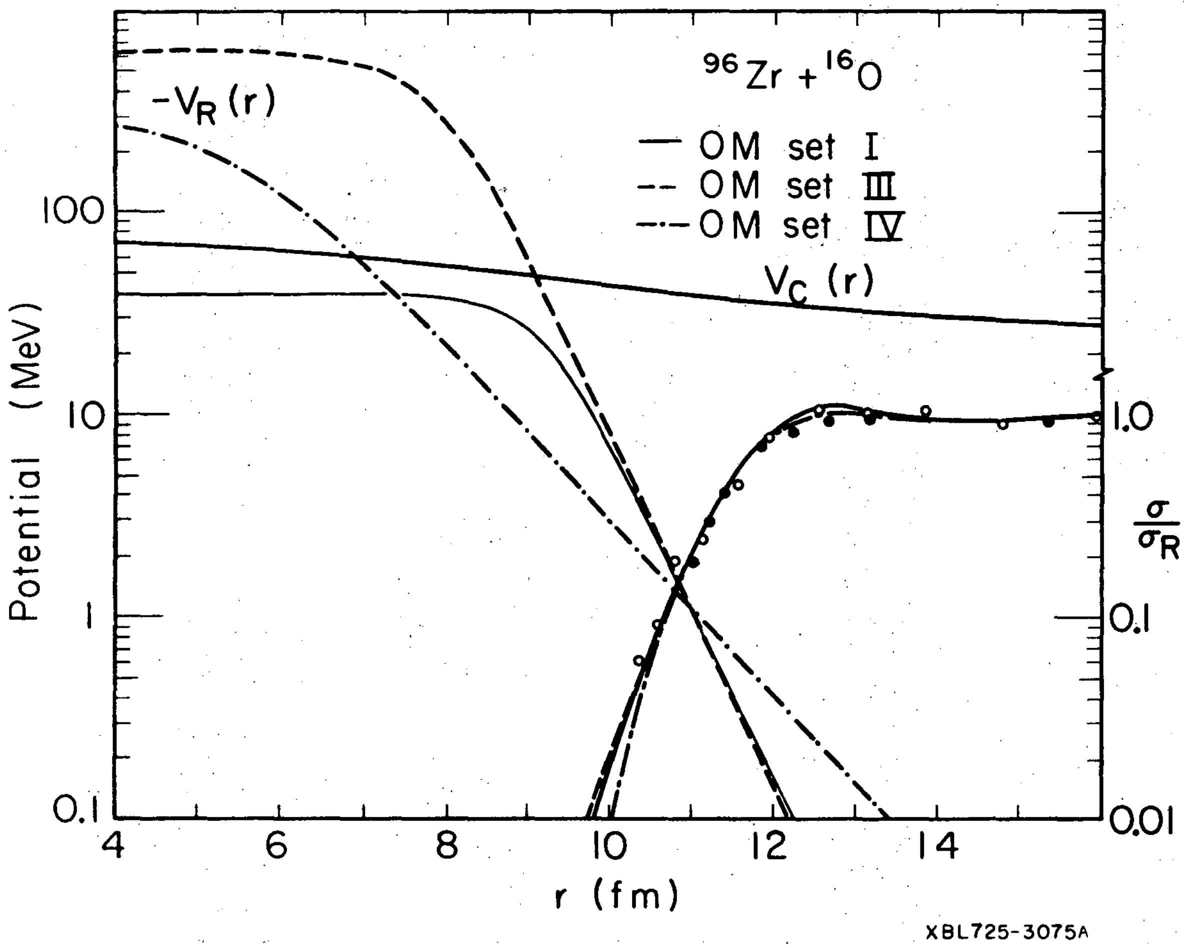
$^{96}Zr + ^{16}O$
$-V_R(r)$
OM set I
OM set III
OM set IV
$V_C(r)$
Potential (MeV)
100
10
1
0.1
4
6
8
10
12
14
r (fm)
$\frac{\sigma}{\sigma_R}$
1.0
0.1
0.01
XBL725-3075A

Fig. 6

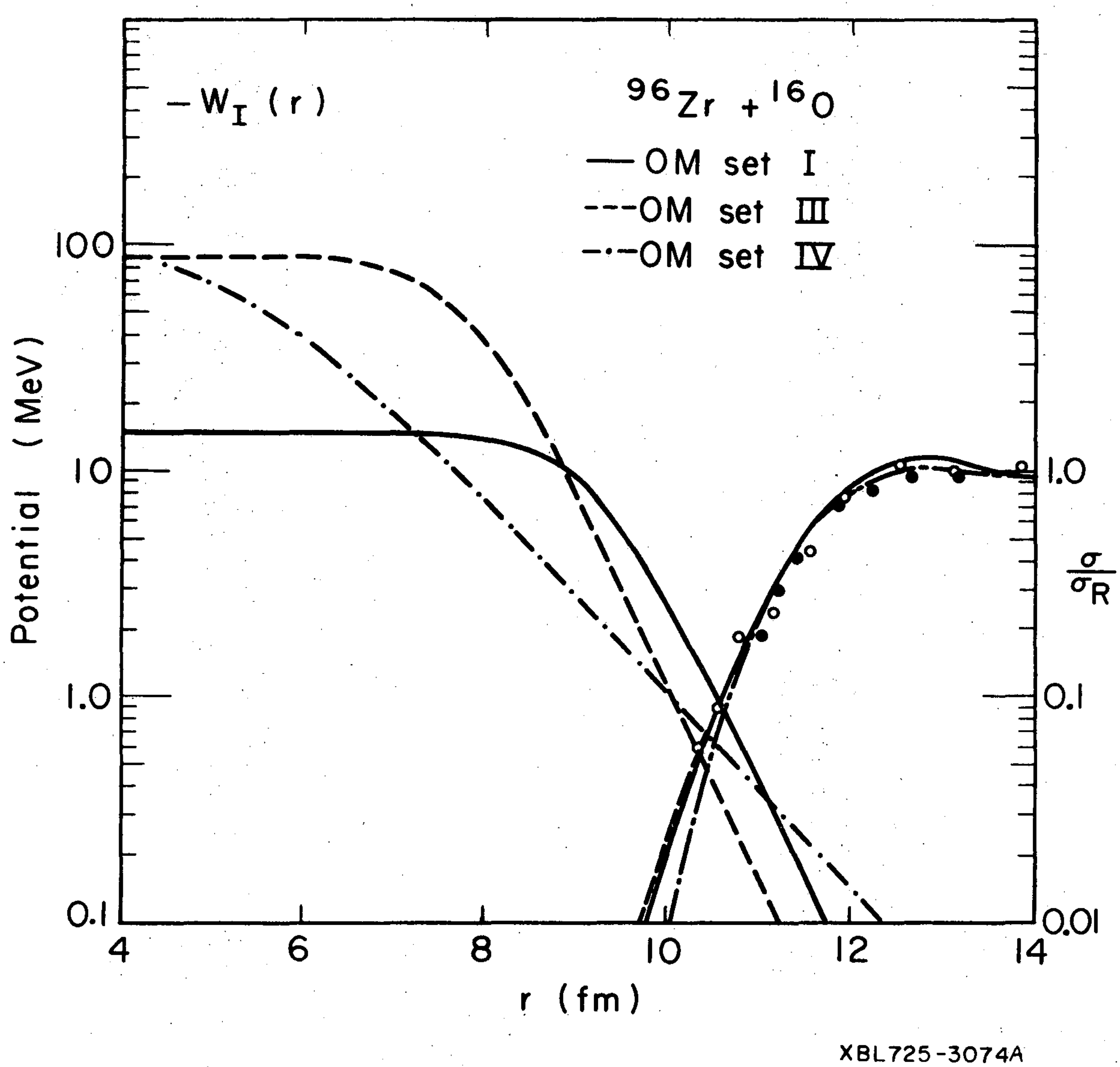

−W_I (r)
96Zr + 16O
OM set I
OM set III
OM set IV
Potential (MeV)
100
10
1.0
0.1
1.0
0.1
0.01
σ/σR
4
6
8
10
12
14
r (fm)
XBL725-3074A

Fig. 7

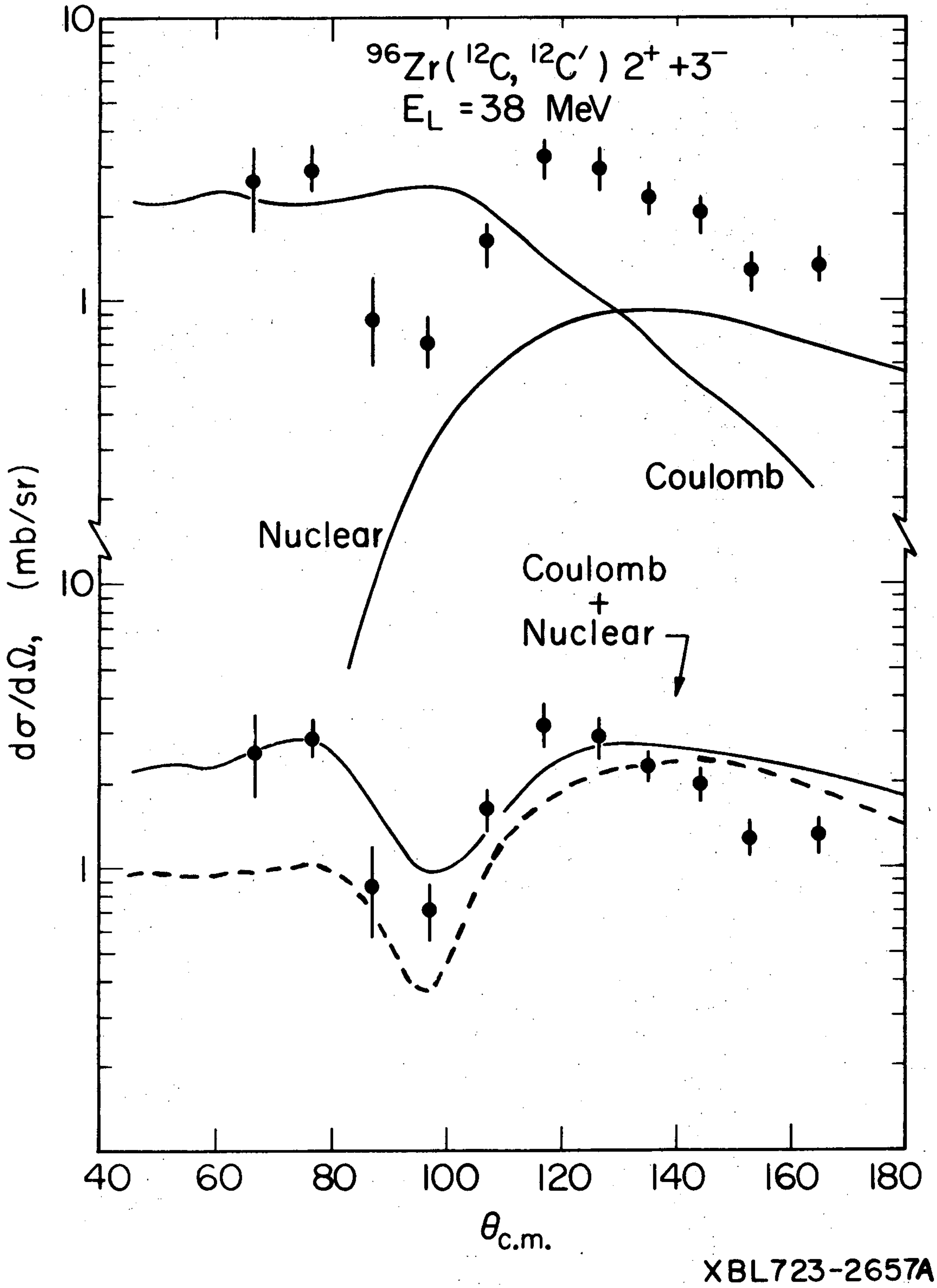
$^{96}Zr(^{12}C, ^{12}C')\ 2^+ + 3^-$
$E_L = 38$ MeV
Coulomb
Nuclear
Coulomb + Nuclear
$d\sigma/d\Omega$, (mb/sr)
10
1
10
1
40
60
80
100
120
140
160
180
$\theta_{c.m.}$
XBL723-2657A

Fig. 8

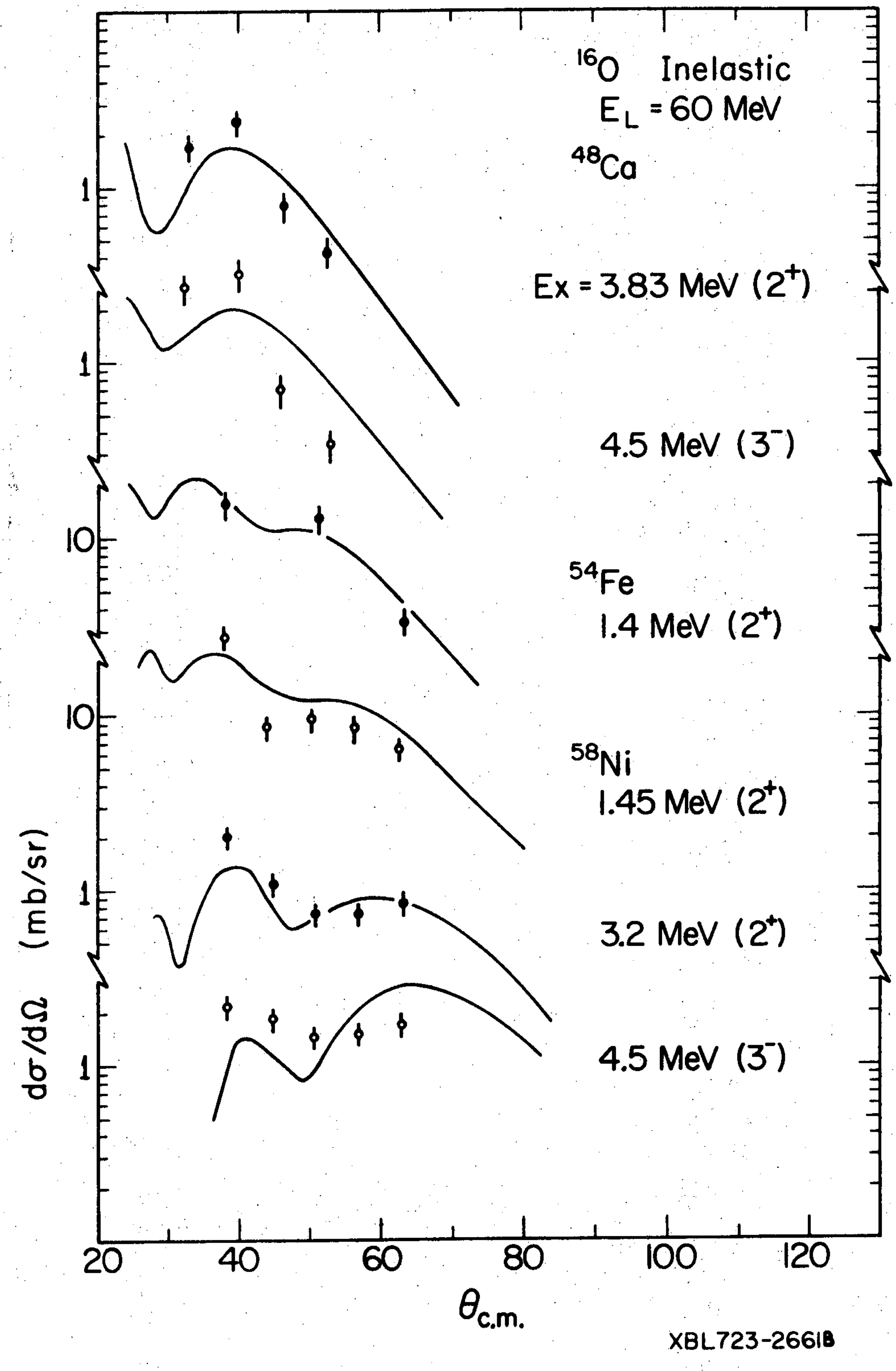

16O Inelastic
EL = 60 MeV
48Ca
Ex = 3.83 MeV (2+)
4.5 MeV (3-)
54Fe
1.4 MeV (2+)
58Ni
1.45 MeV (2+)
3.2 MeV (2+)
4.5 MeV (3-)
1
1
10
10
1
1
dσ/dΩ (mb/sr)
20
40
60
80
100
120
θc.m.
XBL723-2661B

Fig. 9

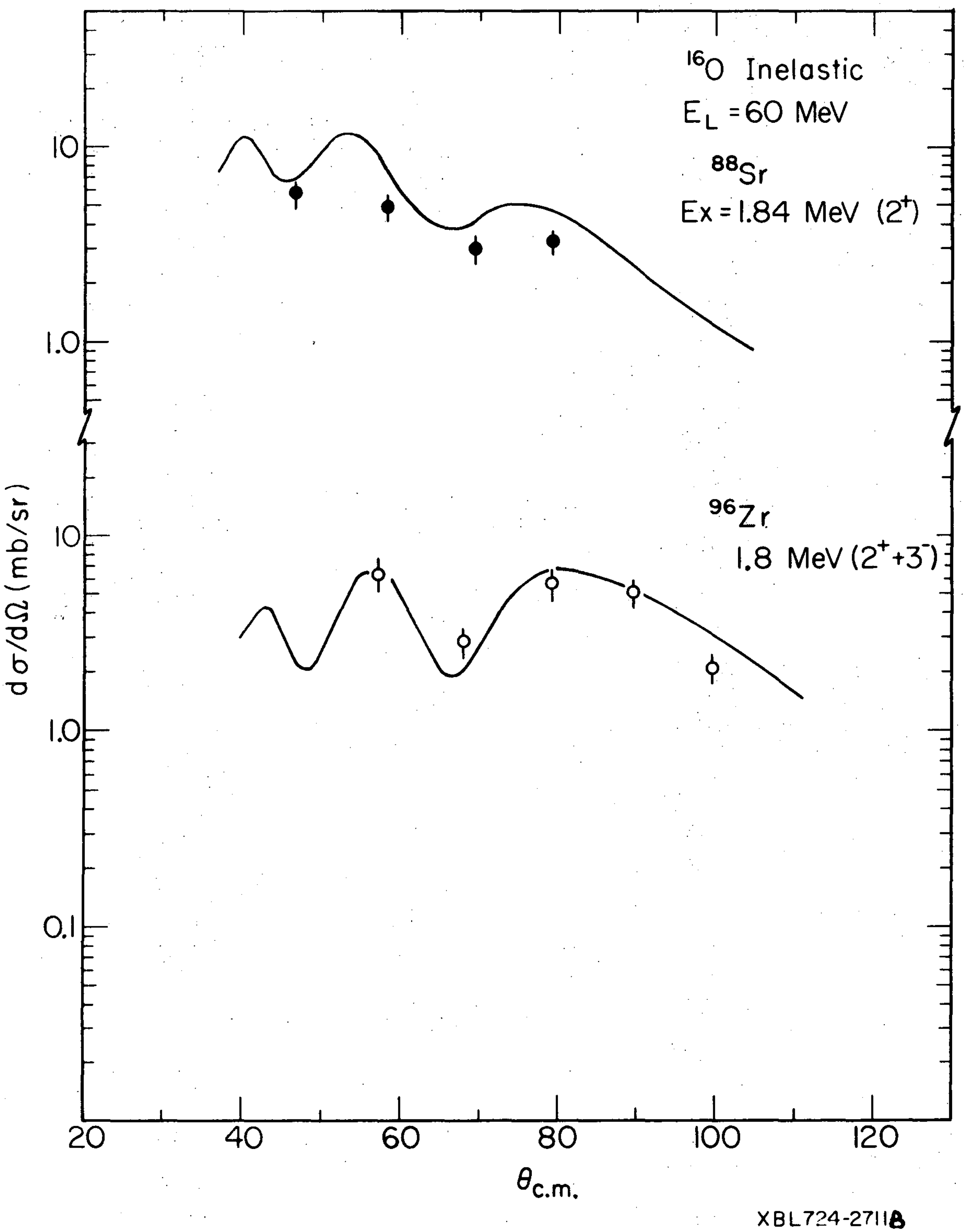

^{16}O Inelastic
$E_L = 60$ MeV
^{88}Sr
Ex = 1.84 MeV (2^+)
^{96}Zr
1.8 MeV ($2^+ + 3^-$)
10
1.0
10
1.0
0.1
$d\sigma/d\Omega$ (mb/sr)
20
40
60
80
100
120
$\theta_{c.m.}$
XBL724-2711B

Fig. 10

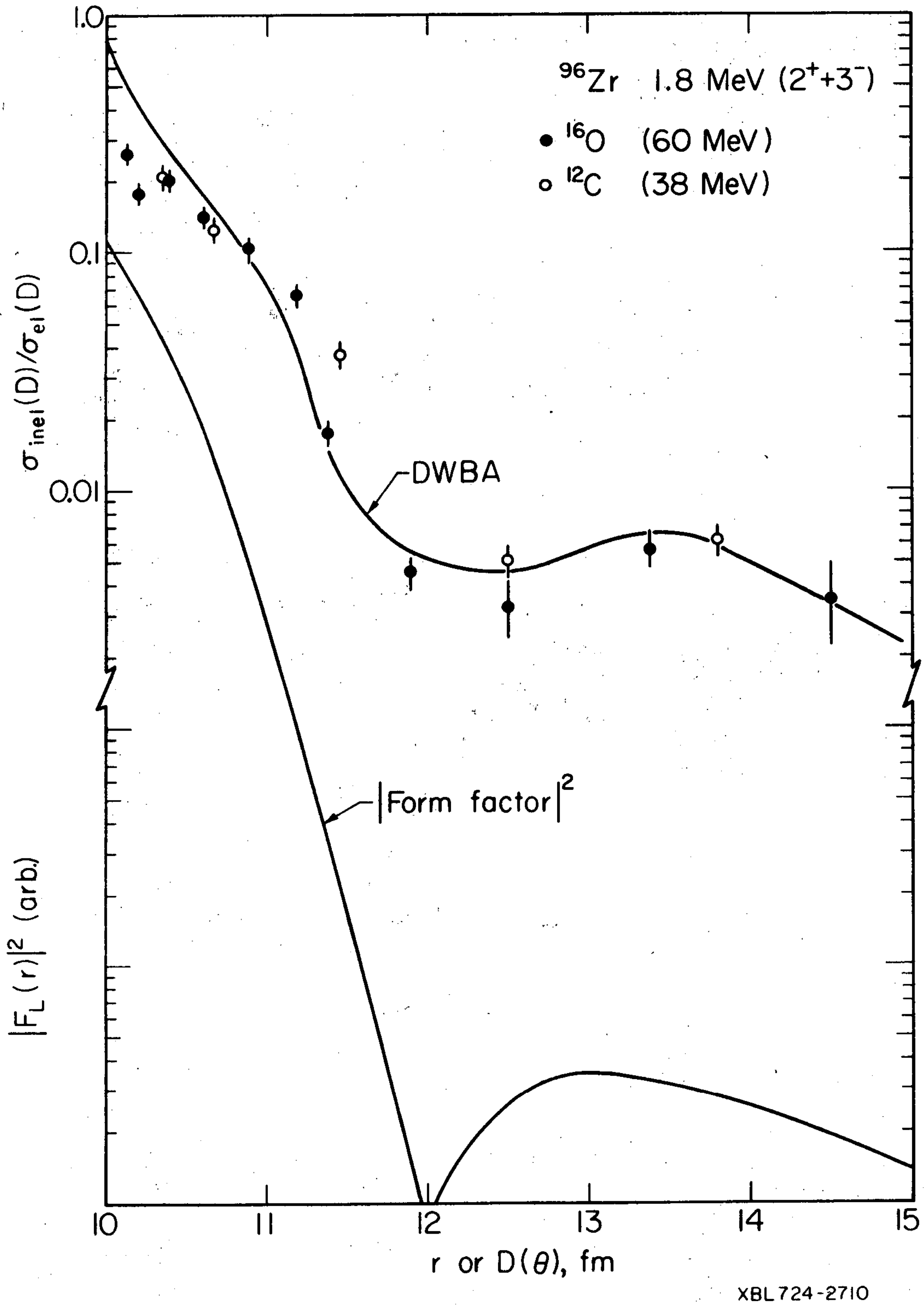

1.0
0.1
0.01
^{96}Zr 1.8 MeV (2$^+$+3$^-$)
● ^{16}O (60 MeV)
○ ^{12}C (38 MeV)
DWBA
|Form factor|^2
$\sigma_{inel}(D)/\sigma_{el}(D)$
$|F_L(r)|^2$ (arb.)
10
11
12
13
14
15
r or D(θ), fm
XBL 724-2710

Fig. 11

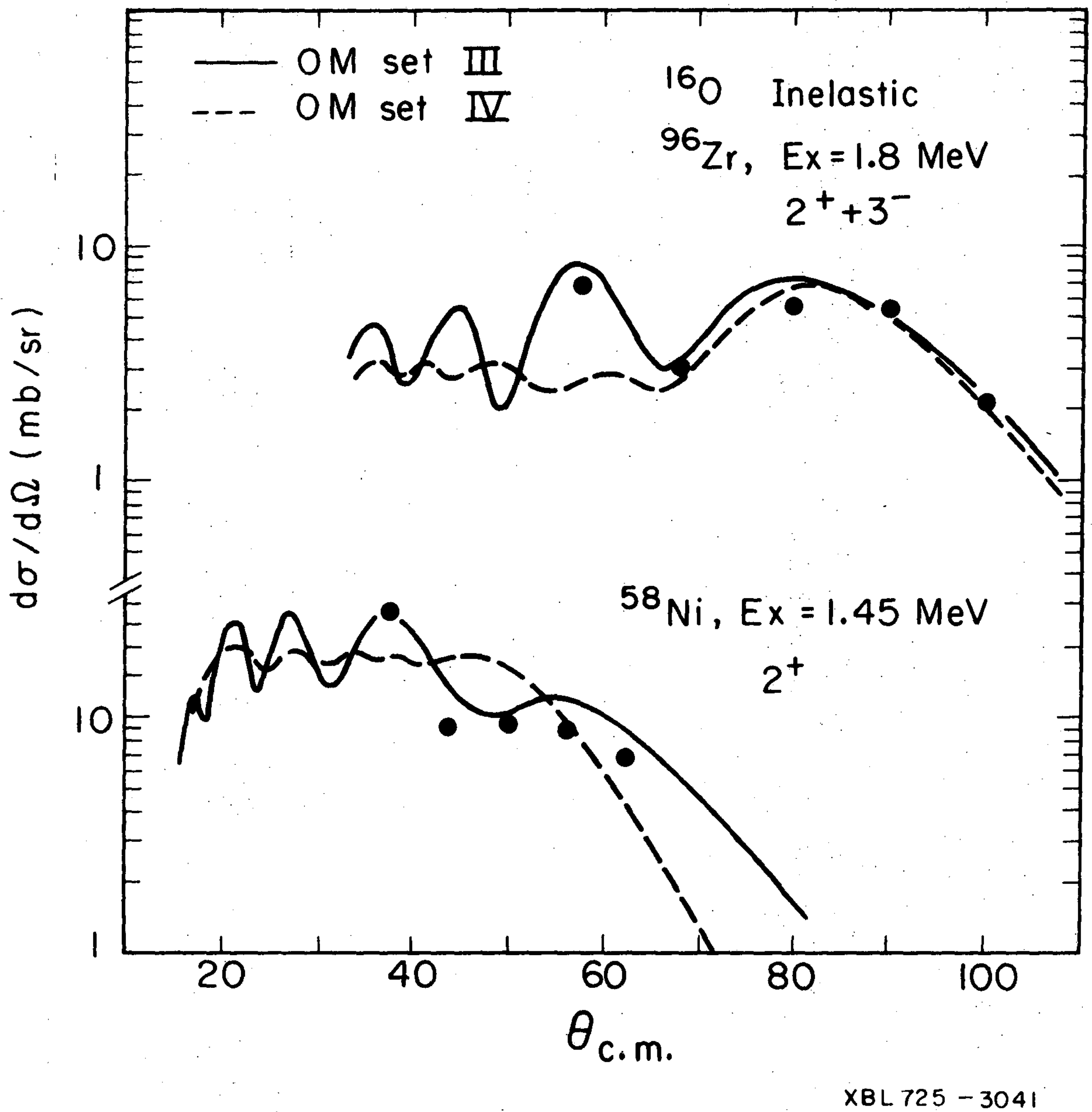
OM set III
OM set IV
^{16}O Inelastic
^{96}Zr, Ex = 1.8 MeV
2^{+}+3^{-}
^{58}Ni, Ex = 1.45 MeV
2^{+}
dσ/dΩ (mb/sr)
10
1
10
1
20
40
60
80
100
θ$_{c.m.}$
XBL 725 - 3041

Fig. 12

TECHNICAL INFORMATION DIVISION
LAWRENCE BERKELEY LABORATORY
UNIVERSITY OF CALIFORNIA
BERKELEY, CALIFORNIA 94720